Tensor Gradient L_0-Norm Minimization-Based Low-Dose CT and Its Application to COVID-19

Weiwen Wu, Jun Shi, *Associate Member, IEEE*, Hengyong Yu, *Senior Member*, *IEEE,* Weifei Wu, and Varut Vardhanabhuti

***Abstract*— Methods to recover high-quality computed tomography (CT) images in low-dose cases will be of great benefit. To reach this goal, sparse-data subsampling is one of the common strategies to reduce radiation dose, which is attracting interest among the researchers in the CT community. Since analytic image reconstruction algorithms may lead to severe image artifacts, the iterative algorithms have been developed for reconstructing images from sparsely sampled projection data. In this study, we first develop a tensor gradient L_0-norm minimization (TGLM) for low-dose CT imaging. Then, the TGLM model is optimized by using the split-Bregman method. The Coronavirus Disease 2019 (COVID-19) has been sweeping the globe, and CT imaging has been deployed for detection and assessing the severity of the disease. Finally, we first apply our proposed TGLM method for COVID-19 to achieve low-dose scan by incorporating the 3-D spatial information. Two COVID-19 patients (64 years old female and 56 years old man) were scanned by the μCT 528 system, and the acquired projections were retrieved to validate and evaluate the performance of the TGLM.**

***Index Terms*— Chest CT, Coronavirus Disease 2019 (COVID-19), low-dose computed tomography (CT), tensor gradient L_0-norm.**

I. INTRODUCTION

FOR X-ray computed tomography (CT), how to reduce the radiation dose has been attracting great attention as lower radiation dose means lower risks of radiation-related effects [1]. Sparse-view CT is one of the low-dose CT reconstructions by collecting the number of projections. As only the insufficient projection views are collected, it results in sparse-view CT producing severe streaking artifacts in filtered backprojection (FBP) reconstruction. To overcome this challenge, the compressed sensing approaches that minimize the total variation (TV) or other deep learning-based methods were developed [2], [3]. However, most of the approaches were proposed for fan-beam or cone-beam geometry, which are difficult to be implemented in clinical practice.

In order to satisfy Tuy's condition [4], modern commercial chest CT systems usually adopt helical geometry to reconstruct the scanned object exactly [5]. To reconstruct images from measurements, general analytic algorithms may be a good choice to implement image reconstruction for complete projections [6], [7]. However, due to the radiation dose reduction (for example, sparse-view case), the image reconstruction would be a typical ill-posed inverse problem [8], [9], which can introduce artifacts in the reconstructed images if we employ the analytic methods. Until now, many efforts have been contributed to low-dose CT imaging [10], [11], including dictionary learning reconstruction [12], [13], edge-preserving TV [14], artificial neural network [15], discriminative feature representation [16], domain progressive 3-D residual convolution network [17], deep iterative reconstruction estimation [18], and residual encoder–decoder convolutional neural network [19]. Unfortunately, most of these methods are developed for 2-D scanning geometry rather than for helical geometry. When these methods are extended to helical imaging, they would confront a series of problems, including parameters selection, sparsity transform, and spatial domain mapping.

As for the helical CT reconstruction, previous approaches mainly concentrate on analytic reconstruction, such as FBP. With recent advances in computing performance, a traditionally computationally intensive method, such as iterative reconstruction, can now be reconsidered. Indeed, there were some efforts to develop advanced iteration methods, including model-based iterative reconstruction [20], [21], modified ordered subsets [22], and adaptive statistical iterative reconstruction technique [23]. By incorporating prior knowledge into a reconstruction model, higher order variation [24] methods were proposed. To further improve the image quality in low-dose case, the tensor framelet-based method was extended from dynamic CT to helical CT [25]. However, all of these methods ignore two important features for helical CT imaging. One is that the adjacent slices share similar image structures and features. The other is that the materials usually maintain continuous along the z-axis from material tissue view. According to the correlation between energy magnitude and material attenuation, the intensity on the z-axis direction can also be similar.

Manuscript received October 20, 2020; revised December 15, 2020; accepted December 30, 2020. Date of publication January 19, 2021; date of current version February 16, 2021. This work was supported in part by the Li Ka Shing Foundation and in part by the National Natural Science Foundation of China under Grant 61801336. The Associate Editor coordinating the review process was Adam G. Polak. *(Corresponding authors: Weifei Wu; Varut Vardhanabhuti*.)

Weiwen Wu and Varut Vardhanabhuti are with the Department of Diagnostic Radiology, The University of Hong Kong, Hong Kong, China (e-mail: weiwenwu12@gmail.com; varv@hku.hk).

Jun Shi is with the School of Communication and Information Engineering, Shanghai Institute for Advanced Communication and Data Science, Shanghai University, Shanghai 200444, China.

Hengyong Yu is with the Department of Electrical and Computer Engineering, University of Massachusetts Lowell, Lowell, MA 01854 USA.

Weifei Wu is with the People's Hospital of China Three Gorges University, Yichang 443000, China, and also with the First People's Hospital of Yichang, Yichang 443000, China (e-mail: wuweifei236@sina.com).

Digital Object Identifier 10.1109/TIM.2021.3050190

The image gradient L_0-norm minimization within the 2-D spatial domain was proposed for image smoothing [26] by calculating a nonzero number of gradient images. Then, it was widely used in image deblurring, image segmentation, sparse linear hyperspectral unmixing [27], and so on. Besides, image gradient L_0-norm minimization-based reconstruction techniques gained significant interest in low-dose CT reconstruction [28]–[30]. This type of image gradient L_0-norm minimization is constrained with the 2-D spatial domain. However, we usually encounter such cases, including hyperspectral image recovery [31], hyperspectral image denoising [32], and dynamic spectral CT reconstruction [29], [33], [34]. In such cases, because the measurements are higher order tensors rather than 2-D signals, the referred image gradient L_0-norm may fail. Again, we need to renew the image gradient L_0-norm as a general tensor format, which is a focus in this work. Because it is proposed for higher order tensor, it can be called a tensor gradient L_0-norm naturally.

The Coronavirus Disease 2019 (COVID-19) was discovered in December 2019 and then rapidly spread around the world with severe health and economic consequences [35]. Ways to curb this disease development and protect the health of infected people has become a common issue for all mankind. COVID-19 has some imaging features for CT image [7], which is helpful for the radiologist early detection and diagnosis. These features mainly include involvement of more than two lobes, ground-glass opacities, opacities with rounded morphology, a peripheral distribution of disease, consolidation with ground-glass opacities, and crazy-paving pattern [36]. CT has proved useful for early detection even in asymptomatic patients, as well as for assessing disease severity. Therefore, it is not uncommon that patients may require several scans during the same hospital episodes, particularly if the symptoms are worsening. In this case, the radiation dose becomes a major concern, especially for young patients and pregnant women. As for COVID-19 patient, imaging features are detectable, which are good for diagnosis in clinics. However, at very low dose, artifacts may occur, which will mask these imaging features. To guarantee the accuracy of diagnosis, it is important to retain those COVID-19 unique image features with artifacts suppression. To demonstrate the feasibility of the TGLM method, it is employed to COVID-19 patients in low-dose cases.

The contributions can be summarized in the following three points. First, we propose and establish the tensor gradient L_0-norm tensor recovery model and validate the advantages over 2-D image gradient L_0-norm. Second, we establish a tensor gradient L_0-norm minimization (TGLM)-based low-dose CT imaging model to characterize the sparsity of chest CT images. Finally, the split-Bregman method is employed to optimize the proposed TGLM model. Specifically, closed-form equations of separate variables are deduced so that the implementation is much clearer. Finally, it is employed to realize the goal of low-dose reconstruction for COVID-19 patients.

The rest of this study is organized as follows. In Section II, we will briefly introduce the basic theories of helical CT, analyze the unique imaging features of COVID-19 patients, and establish the TGLM-based tensor recovery model. We will also establish the TGLM model and optimization procedures. In Section III, the clinical data set from COVID-19 patients is employed to evaluate the TGLM and other comparisons. In Section IV, we will discuss the related issues and the conclusion for this study.

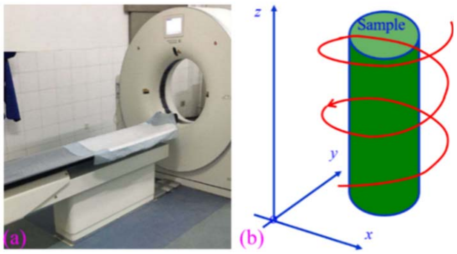

Fig. 1. Imaging system. (a) Photograph of a μCT 528 system. (b) Illustration of helical scanning geometry.

II. CT IMAGING AND TGLM

A. Imaging Scheme

Fig. 1(a) shows a μCT 528 system manufactured by Shangai United Imaging Healthcare Company Ltd., which is employed to collect clinical experimental data sets. This system is a multislice X-ray CT scanner featuring a continuously rotating tube–detector pair. The scanning mode is set as helical [see Fig. 1(b)].

Assuming that the imaging object center is the origin, the helical locus can be expressed as

$$\mathscr{P}(m) = \left(s_1 \times \cos\frac{2\pi m}{M}, s_1 \times \sin\frac{2\pi m}{M}, s_2\{\times\}\frac{m}{M}\right) \tag{1}$$

where s_1 is the distance starting from X-ray source to transaxis passing through the origin, s_2 is the pitch that is the distance of patient table moving per rotation, M represents the total views per rotation, and m is the view index.

B. Tensor Gradient L0-Norm

1) 2D Image Gradient L0-Norm Minimization: For a given 2-D image $\mathbf{X} \in \mathbb{R}^{I_1 \times I_2}$, where I_1 and I_2 represent the height and width of the image, a general form of its TV can be given as

$$\|\nabla \mathbf{X}\|_1 = \sum_{i_1=1}^{I_1}\sum_{i_2=1}^{I_2}\left(|\partial_{x_1}\mathbf{X}|+|\partial_{x_2}\mathbf{X}|\right) \tag{2}$$

where $\mathbf{X}(i_1, i_2)$represent the $(i_1,i_2)^{th}$element, $\partial_{x_1}\mathbf{X} = \mathbf{X}(i_1, i_2) - \mathbf{X}(i_1 - 1, i_2)$, and $\partial_{x_2}\mathbf{X} = \mathbf{X}(i_1, i_2) - \mathbf{X}(i_1, i_2 - 1)$. From (1), we can see that TV considers the summation of the magnitude of the image gradient. To enhance high-contrast edges by counting the number of nonzero gradients, the gradient L_0-norm was proposed and it can be defined as [26]

$$\|\nabla \mathbf{X}\|_0 = \sum_{i_1=1}^{I_1}\sum_{i_2=1}^{I_2} g\left((i_1, \quad i_2)\lfloor|\partial_{x_1}\mathbf{X}|+|\partial_{x_2}\mathbf{X}|\neq 0\rfloor\right) \tag{3}$$

where $g(i_1, i_2)$ is the counting operation on $\mathbf{X}$. When $(i_1, i_2)^{th}$ location of $\mathbf{X}$ satisfy $|\mathbf{X}(i_1, i_2)-\mathbf{X}(i_1 - 1, i_2)|+|\mathbf{X}(i_1, i_2)-\mathbf{X}(i_1, i_2 - 1)| \neq 0$, the value of $g(i_1, i_2)$ would add one. From (2), one can see that the small amplitudes can be retained by image gradient L_0-norm. It is good for image edge preservation and details recovery. Thus, 2-D image gradient L_0-norm was widely used in image recovery, image reconstruction, image enhance, image inpaiting [37], and so on.

2) Tensor Gradient L0-Norm Model: The referred L_0-norm minimization has obtained great success, and it can provide high efficiency for 2-D images. However, if it is employed to color image smoothing, the correlations among different channels would be ignored. In fact, it is usually to address such problems, including spectral CT reconstruction, hyperspectral remote sensing, video recovery/smoothing/denoising/blurring, and volumetric image recovery. In this case, there are strong correlations among different channels. For example, the image structures and details from different channels are very similar for hyperspectral and spectral CT images. The image structures and details from the video are also continuous. To address these problems, a tensor form of gradient L_0-norm is of great significance. In general, given an $N-$ order tensor $\boldsymbol{X} \in \mathbb{R}^{I_1\times I_2\times\ldots\times I_N}$, tensor gradient L_0-norm can be defined as

$$\|\nabla\mathcal{X}\|_0=\sum_{i_N=\mathbf{1}}^{I_N}\cdots\sum_{i_1=\mathbf{1}}^{I_1}g\big((i_1,i_2,\ldots,i_N)\lfloor|\partial_{x_1}\mathcal{X}| +\ldots+|\partial_{x_N}\mathcal{X}|\neq\mathbf{0}\rfloor\big) \tag{4}$$

where $\partial_{x_n}\mathcal{X} = \mathcal{X}(i_1,\ldots,i_n,\ldots,i_N) - \mathcal{X}(i_1,\ldots,i_n - 1,\ldots,i_N), (n = 1,\ldots,N)$. From (3), the tensor gradient L_0-norm can count nonzero number from different directions. This means that the recovery tensor should satisfy this strong constraint, which is good for pursuing a more stable and optimized solution. In order to clarify this point, we can discuss a general tensor recovery problem

$$\min_{\boldsymbol{x}}\|\nabla\mathcal{X}\|_0,\quad st., \mathcal{Y}=\mathcal{X}+\mathcal{E} \tag{5}$$

where $\mathcal{Y} \in \mathbb{R}^{I_1\times I_2\times\ldots\times I_N}$ is the measured tensor and $\mathcal{E} \in \mathbb{R}^{I_1\times I_2\times\ldots\times I_N}$ is the system noise. Equation (4) is a constraint optimization problem, which can be converted into the following unconstrained problem:

$$\min_{\boldsymbol{x}}\frac{1}{2}\|\mathcal{Y}-\mathcal{X}\|_F^2+\lambda\|\nabla\mathcal{X}\|_0 \tag{6}$$

where $\lambda > 0$ is the regularization factor. Actually, (6) can be written as

$$\min_{\boldsymbol{x}}\frac{1}{2}\sum_{i_N=1}^{I_N}\cdots\sum_{i_1=1}^{I_1}\big\{(\mathcal{Y}(i_1,i_2,\ldots,i_N)-\mathcal{X}(i_1,i_2,\ldots,i_N))^2 +\lambda g\big((i_1,i_2,\ldots,i_N)\lfloor|\partial_{x_1}\mathcal{X}|+\ldots+|\partial_{x_N}\mathcal{X}|\neq 0\rfloor\big)\big\} \tag{7}$$

where $\mathcal{Y}(i_1, i_2,\ldots, i_N)$ and $\mathcal{X}(i_1, i_2,\ldots, i_N)$ representthe $(i_1, i_2,\ldots, i_N)^{th}$ entry of $\mathcal{Y}$ and $\mathcal{X}$. From (3), one can observe that $\partial_{x_n}\mathcal{X}(n = 1,\ldots, N)$ corresponds the gradient tensor along the x_n^{th} dimension. Therefore, we can use N auxiliary tensors $\{\mathcal{G}_n\}_{n=1}^N$ to replace $\{\partial_{x_n}\mathcal{X}\}_{n=1}^N$. Equation (7) can be converted into the following constraint optimization problem:

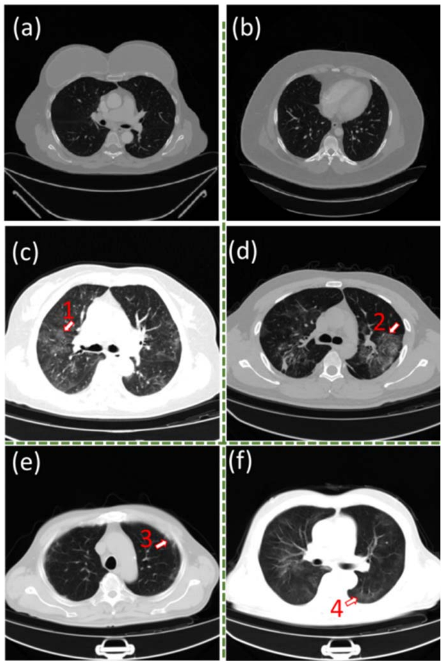

Fig. 2. (a) and (b) Two representative slices from healthy CT human (c)–(f) Representative image features from four different COVID-19 patients within appropriate display widows. Note that these COVID-19 patients are obtained from the People's Hospital of China Three Gorges University (Yichang), Hubei, China.

$$\begin{aligned}\min_{\boldsymbol{x},\{\mathcal{G}\}_{n=1}^N}\ &\frac{1}{2}\sum_{i_N=1}^{I_N}\cdots\sum_{i_1=1}^{I_1}\{(\mathcal{Y}(i_1,i_2,\ldots,i_N)\\ &-\mathcal{X}(i_1,i_2,\ldots,i_N))^2+\lambda g((i_1,i_2,\ldots,i_N)\lfloor|\mathcal{G}_1|\\ &+\ldots+|\mathcal{G}_N|\neq\mathbf{0}\rfloor)\}\\ \text{st.},&\mathcal{G}_n=\partial_{x_n}\mathcal{X},\quad n=1,\ldots,N.\end{aligned} \tag{8}$$

Equation (8) can be further converted into the following unconstrainted problem under some fixed conditions. We have

$$\begin{aligned}\min_{\boldsymbol{x},\{\mathcal{G}_n\}_{n=1}^N}&\frac{1}{2}\sum_{i_N=1}^{I_N}\cdots\sum_{i_1=1}^{I_1}\big\{(\mathcal{Y}(i_1,i_2,\ldots,i_N)-\mathcal{X}(i_1,i_2,\ldots,i_N))^2\\ &+\lambda g((i_1,i_2,\ldots,i_N)\lfloor|\mathcal{G}_1|+\ldots+|\mathcal{G}_N|\neq\mathbf{0}\rfloor)\}\\ &+\frac{1}{2}\sum_{n=1}^{N}\beta_n\|\mathcal{G}_n-\partial_{x_n}\mathcal{X}\|_F^2\end{aligned} \tag{9}$$

where $\beta_n(n = 1,\ldots, N)$ represents the coupling factor from n^{th} gradient tensor, which can be considered a parameter to balance the proportion of all gradient tensors. More details of the solution can refer to Appendix A.

C. COVID-19 CT Image Features

The imaging features from COVID-2019 are typically of bilateral parenchymal ground-glass opacities of peripheral locations [see Fig. 2(a)–(d)]. From Fig. 2, one can observe that those COVID-2019 image features may occupy small areas compared with larger normal areas on CT images, especially

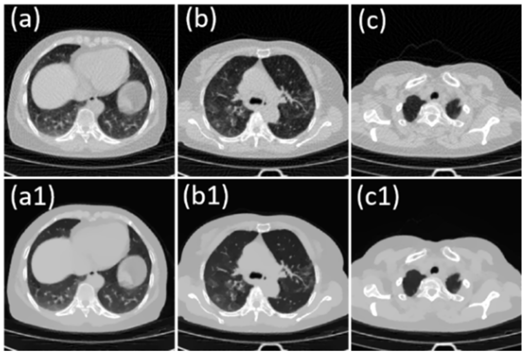

Fig. 3. Recovering results of three representative CT slices (40th, 100th, and 140th slices) of patient #1 using TGLM method. (a)–(c) and (a1)–(c1) represent the SIRT and TGLM results from an undersampling factor 12.

in mild COVID-19 patient. In such cases, advanced helical CT reconstruction methods will be necessary to reconstruct high-quality images without missing these features. In addition, the unique COVID-19 features may be very similar to artifacts from the image analysis aspect, especially in the low-dose case. To this end, it is important to maintain image quality so that appearance of ground-glass opacity can be differentiated from artifacts, even at low dose. Once ground-glass opacity can be confidently diagnosed by physicians, then further accurate interpretation can be made, but it is acknowledged that ground-glass opacity appearance in itself is not specific to COVID-19. Combination with typical clinical symptoms, location of opacities, and further quantitative analysis may improve specificity for the diagnosis, and more details refer to our recent work [38].

D. Tensor Gradient L0-Norm Application

COVID-2019 CT images can be treated as a third-order tensor. Thus, in theory, it can be recovered by the TGLM method with reduced artifacts from low-dose measurements. Note that the original images are reconstructed by simultaneous iterative reconstruction technique (SIRT) [39]. Then, the images are recovered by minimizing (5). Here, assuming that the undersampling factor is 12 (it will be discussed in Section IV-A), three representative slices by using the TGLM are given in Fig. 3. From Fig. 3, we can observe that the TGLM can remove the artifacts by incorporating 3-D prior. However, some finer details are also missing in the TGLM results.

The TGLM mainly focuses on image sparsity within tensor space because the TGLM can not only characterize the image sparsity within 2-D space but also explore the sparsity along the z-axis. This is consistent with piecewise constant property of CT images [40]. When there are sparse-view artifacts within CT image, such piecewise constant property would be corrupted with poor image quality. Again, the TGLM characterizes the 3-D image structure prior by considering the sparsity within 3-D space. To further obtain better results for imaging, such 3-D image structure prior is incorporated into an image reconstruction model. Hence, we introduce the TGLM into reconstruction to establish a unified image reconstruction model.

III. TGLM-BASED IMAGE RECONSTRUCTION

The modern helical CT scanner can collect data from the whole X-ray emitting energy spectrum, and the goal of image reconstruction is to recover high-quality CT images from the measurements. The ideal forward model for helical cone-beam geometry can be expressed as

$$\mathcal{M}\mathbf{z} = \mathcal{P} + \mathcal{E}_1. \tag{10}$$

Here, $\mathcal{M} \in \mathbb{R}^{C\times J}(C = C_1 \times C_2 \times C_3)$ is the system forward transform, C_1 and C_2 are the number of row and column of the used detector, and C_3 and J represent the number of projections and reconstruction pixels. $\mathbf{z} \in \mathbb{R}^J$ is the vectorization of reconstructed image tensor $\mathcal{Z} \in \mathbb{R}^{J_1\times J_2\times J_3}$ ($J = J_1 \times J_2 \times J_3$), where J_1, J_2, and J_3 represent the height, width, and depth of the 3-D image, respectively. $\mathcal{P} \in \mathbb{R}^C$ and $\mathcal{E}_1 \in \mathbb{R}^C$ represent measurements and noise. Because $\mathcal{M}$ usually is too huge, (10) cannot be solved using a direct inversion transform. The iterative methods are usually used to minimize the following problem:

$$\min_{z} \frac{1}{2}\|\mathcal{M}\mathbf{z} - \mathcal{P}\|_F^2 \tag{11}$$

where $\|\cdot\|_F$ represents the Frobenius norm of the tensor. There are some classic methods to solve (11), including algebraic reconstruction technique (ART) [41] and SIRT [39]. Equation (11) is a typical ill-posed inverse problem, especially in low-dose case. Incorporating prior knowledge into this model can be a good strategy. Here, the proposed tensor gradient L_0-norm is considered and its mathematical model can be established as

$$\min_{z} \frac{1}{2}\|\mathcal{M}\mathbf{z} - \mathcal{P}\|_F^2 + \eta\|\nabla\mathcal{Z}\|_0 \tag{12}$$

where $(1/2)\|\mathcal{M}\mathbf{z} - \mathcal{P}\|_F^2$ and $\|\nabla\mathcal{Z}\|_0$ represent data fidelity and regularization prior term, respectively, and η is a regularization parameter. To further optimize the object function of (12), the split-Bregman method is employed here. First, we introduce an auxiliary variable $\mathcal{W}$ to replace $\mathcal{Z}$, and (12) can be converted into the following constraint optimization problem:

$$\min_{z,w} \frac{1}{2}\|\mathcal{M} - \mathcal{P}\|_F^2 + \eta\|\nabla\mathcal{W}\|_0, \quad \text{st.}\mathcal{W} = \mathcal{Z}. \tag{13}$$

Equation (13) is a constraint problem, which can be further converted into an unconstrainted optimization problem with the concerned condition. Again, we have

$$\min_{z,w,v} \frac{1}{2}\|\mathcal{M}\mathbf{z} - \mathcal{P}\|_F^2 + \eta\|\nabla\mathcal{W}\|_0 + \frac{\eta_1}{2}\|\mathcal{Z} - \mathcal{W} - \mathcal{V}\|_F^2. \tag{14}$$

More description about the solution of (14) is given in Appendix B.

TABLE I

USED PARAMETERS FOR PATIENT STUDY

Patients	η_1	$\beta(10^{-4})$	γ
Case 1	0.05	3.0	35
Case 2	0.05	3.5	40

IV. EXPERIMENTS AND RESULTS

A. Experiment Preparation

Clinical applications are performed to evaluate the proposed method. As aforementioned, the μCT 528 system is used to collect measurements. For this scanner, the used energy integrated detector consists of 864×40 units, where 864 and 40 are the numbers of column and row, respectively. The tube voltage and tube current are set as 120 kVp and 123 mA, respectively. The exposure time is 0.75 s per rotation. The length of the detector unit along the z-axis is 0.55 mm. The distances starting from the X-ray source to the transaxis and detector are 570 and 962.7 mm, respectively. For one rotation, 1080 projections are collected and the translation distance is 12.5 mm. For low-dose imaging, we define an undersampling factor t. For a specified t, only $1080/t$ projections per rotation are extracted to realize low-dose imaging. In such cases, the radiation dose can be reduced to $1/t$ of normal radiation. Here, $t = 12$ is employed to implement our experiments, which means that the radiation dose will be reduced to 1/12.

A 64-year-old female (case 1) and a 56-year-old man (case 2), both confirmed COVID-19 cases, were scanned with the above parameters. Regarding the image reconstruction, the spatial pixel size and the thickness of each slice are set as 0.59 and 1.5 mm, respectively. The reconstructed image tensor has $512 \times 512 \times 144$ pixels covering $300 \times 300 \times 216$ mm^3. The SIRT and TV-based optimization method (TVM) [42] methods are chosen to make a fair comparison. The ground truth used in experiments is obtained by general FBP from full projections. All reconstruction methods are stopped after 500 iterations. The root-mean-square error (RMSE), structural similarity (SSIM), and feature similarity (FSIM) are employed to make qualitative comparisons. All related regularized parameters from reconstruction methods are optimized by comparing the quantitative results, i.e., RMSE, SSIM, and FSIM. All parameters in the proposed method are summarized in Table I.

B. Patient #1

1) Experiment Results: Fig. 4 shows three representative axial slices reconstructed by all the methods with $t = 12$. From these results, one can see that the SIRT results (second row in Fig. 4) always are tarnished by severe sparse undersampling artifacts, and most of the unique image features are difficult to be observed in these results. TVM (third rows in Fig. 4) can improve the reconstructed image quality with artifact reduction to some extent. However, the COVID-19 unique image features are still blurred. Compared with SIRT and TVM, the proposed TGLM method (fourth row in Fig. 4) improves image quality with clear image edges and details by fully exploring the sparsity of volumetric COVID-19 images.

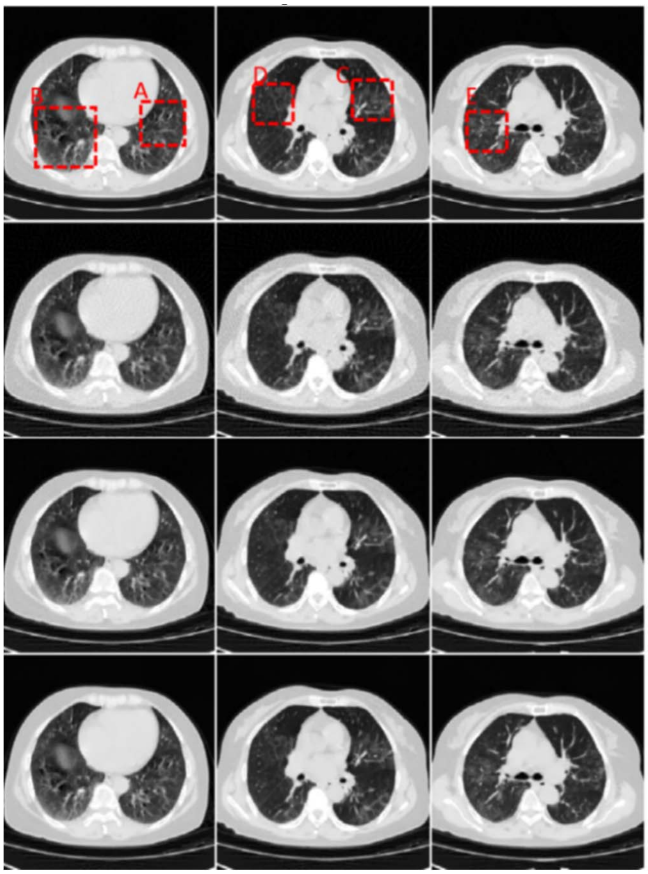

Fig. 4. Reconstructed results for three representative axial slices. First–third columns represent 70th, 105th, and 135th slice, and first–fourth row represent the ground truth, SIRT, TVM, and TGLM results and the window is [−1000, 200] HU.

To demonstrate the advantages of the proposed TGLM algorithm, different regions of interests (ROIs) **“A,” “B,” “C ,” “D,”** and **“E”** are extracted and magnified in Fig. 5. As for the ROI **“A”** results, the image structure marked with the arrows **“1”** is fully masked by artifacts in SIRT results. Although TVM can preserve some clear image edges to some extent, the blocky artifacts make it difficult to discriminate image edges. In comparison, TGLM can provide clear edges.

Regarding the ROI **“B”** results, as shown in Fig. 6, the unique image features are masked by artifacts in SIRT results. Although TVM can recover partial image features to some extent, the blocky artifacts still make it difficult to discriminate image details and features of COVID-19. In comparison, the image structure provided by TGLM can retain the unique features of COVID-19 well with many details.

Related to the ROI **“C”** results, SIRT results (especially in the abdominal area indicated by arrow **“3”** pertaining to vascular structure) contain obvious artifacts and some details are disappeared in Fig. 7. TVM can improve the image quality by removing these artifacts, but small edge lung details as shown here by the outlining for the secondary pulmonary lobule are blurred. The proposed TGLM can provide a clear image structure. This conclusion can be further confirmed by image structure with extracted ROI **“D,”** especially in image structure by arrow **“4.”** Regarding the extracted ROI

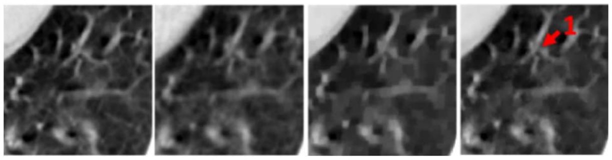

Fig. 5. Magnified ROI A in Fig. 4. First–fourth columns represent ground truth, SIRT, TVM, and TGLM and their windows are [−900, 200] HU.

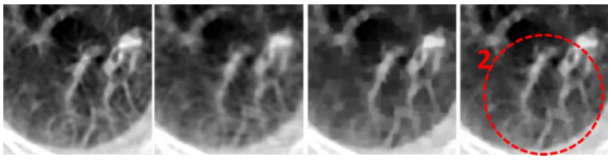

Fig. 6. Similar to Fig. 5 but from Magnified ROI B of Fig. 4. The windows are [−900, 200] HU.

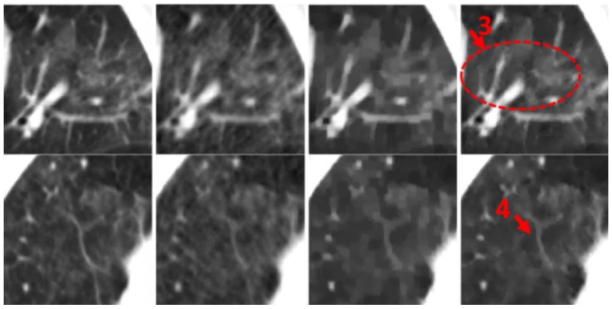

Fig. 7. First and second rows represent the magnified ROIs C and D. First–fourth columns represent reference, SIRT, TVM, and TGLM and the window is [−1000, 0] HU.

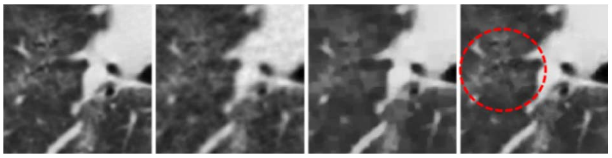

Fig. 8. Similar to Fig. 5 but from magnified ROI E of Fig. 4. The windows is [−1000, 0] HU.

“E” in Fig. 8, the proposed TGLM can also obtain the best reconstruction.

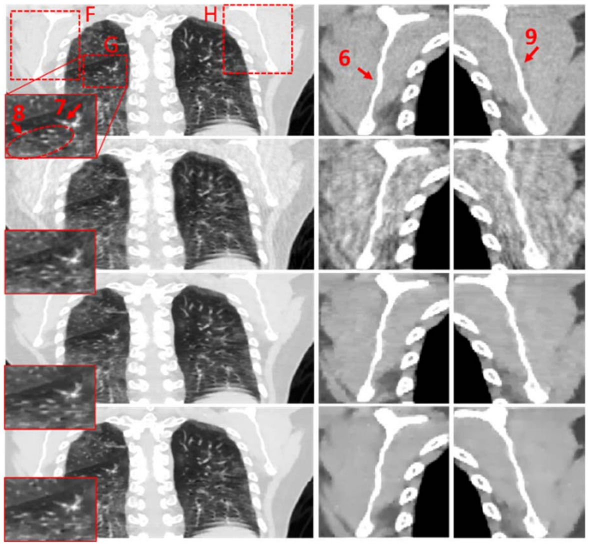

Fig. 9. Reconstructed results from the 370th coronal slice. The first–fourth rows represent the ground truth, SIRT, TVM, and TGLM results. The first column represents reconstructed results and the second–third columns are three ROIs, i.e., ROIs “F” and “H” and their display windows are [−1000, 0], [−200, 200], [−1000, 0], and [−200, 200] HU.

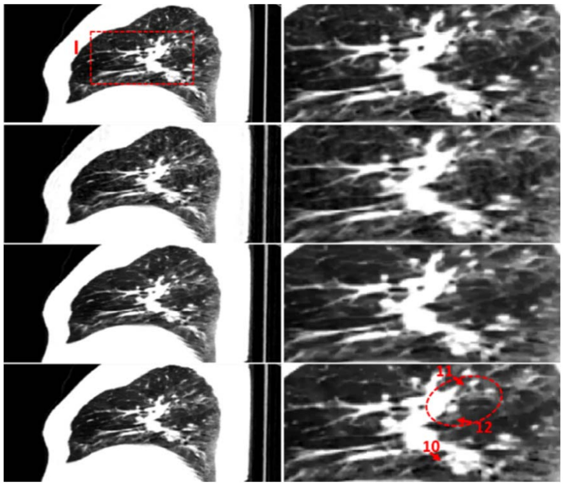

Fig. 10. Reconstructed results from 170th sagittal slice. The first–fourth rows represent the ground truth, SIRT, TVM, and TGLM results. The second column is magnified ROI “I.” The windows of the first–second columns are [−900, 100] HU.

To highlight the advantages of the proposed TGLM algorithm, one representative coronal 370th slice is shown in Fig. 9. From Fig. 9, it can be seen that the TVM and COVID-TGLM can improve the image quality with reduced artifacts. To further compare the performance of TVM and COVID–TGLM, three ROIs **“F,”** **“G,”** and **“H”** are extracted and magnified in the right of Fig. 6. From the ROI **“F”** results, the image quality is degraded by sparse-view artifacts and the image edges are also corrupted. Compared with SIRT results, TVM can improve the image quality a lot; however, the image edges are still corrupted to some extent, especially in image structure indicated by arrow **“6.”** However, these disadvantages can be overcome by the proposed TGLM method. To compare the ability of unique image features recovery with COVID-19 CT imaging, the ROI “G” is magnified in Fig. 9. One can observe that the image edges of lung details by TGLM are much clearer than that those obtained by SIRT and TVM, which can be confirmed by image structure with arrow **“7.”** Especially, the ground-glass opacities in the upper lobes indicated by red oval **“8”** can be observed by our TGLM results, which can further provide an exact clinical diagnosis. From the magnification version of the extracted ROI **“H,”** it can be observed that SIRT contains severe artifacts and they can mask the image edge and details. Compared with TVM and SIRT results, our proposed TGLM can provide better results, which can be confirmed by image structure with arrow **“9.”**

To further highlight the advantages of the proposed TGLM algorithm, the 170th sagittal slice results are shown in Fig. 10 and the ROI **“I”** is further magnified in the second column. From Fig. 10, we can see that the image structure indicated by

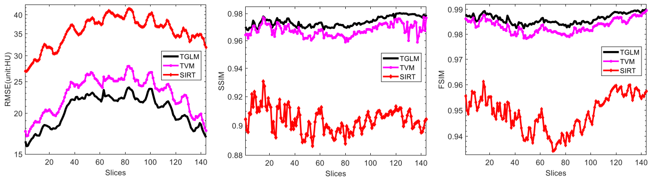

Fig. 11. Quantitative results of all axial slices using different reconstruction methods in terms of RMSE, SSIM, and FSIM.

arrow **"10"** is corrupted in SIRT results and blurred in TVM to some extent. TGLM can improve the resolution with much clearer image edges. The image structure by arrows **"11"** and **"12"** in the ROI **"I"** confirms this conclusion.

To quantitatively compare the performance of all algorithms for COVID-19 imaging, their reconstruction results of all slices from the support lung region are computed with three indexes, i.e., RMSE, SSIM, and FSIM, and they are further given in Fig. 11. Here, the ground truths of all slices are reconstructed by a general FBP algorithm using complete projections. From Fig. 11, one can observe that the proposed TGLM method can achieve the smallest RMSEs for all slices. Due to that no prior knowledge is considered within the SIRT reconstruction model, it has maximum RMSEs value for all slices. Moreover, the results reconstructed by the TVM technique can obtain slightly smaller RMSEs than the SIRT by incorporating prior information into the reconstruction model. Compared with the SIRT and TVM methods, the TGLM has the lowest RMSEs by counting the nonzeros number of third-order tensor gradient rather than penalizing the magnitude of gradient amplitudes in TVM. The SSIM mainly focuses on the similarity between the reconstructed image and ground truth, and it is a common index to compare the performance of different methods [43]. Here, the function of SSIM function is used, where the dynamic range of all channel images is scaled to [0 255], and the constants and window are set as 0.02 and fault value, respectively. FSIM is another metric to evaluate CT image quality [44]. The closer to 1.0 the SSIM and FSIM values are, the better the reconstructed image quality is. It can be seen from Fig. 11 that the proposed TGLM technique can always obtain the greatest SSIM and FSIM values for all slices.

2) Parameters Analysis: There are mainly three parameters η_1, β and γ . To investigate the influence of each parameter on the results, the TGLM results of all slices with one changing parameter and other fixed from the RMSE and SSIM of ROI are computed for analysis. Fig. 12 shows the results of RMSE and SSIM values.

It can be observed from Fig. 12 that the parameters η_1, β and γ play an important role in controlling the reconstructed image quality. Specifically, a better η_1 can reduce RMSE value with greater SSIM value, whereas one smaller or greater η_1 can increase the RMSE and reduce the SSIM. From Fig. 12(a) and (b), we can see that greater RMSEs and smaller SSIMs can be obtained from $\eta_1 = 0.08$ or $\eta_1 = 0.03$ than those that are obtained by $\eta_1 = 0.05$. The quantitative results of different settings of β are given in Fig. 12(c) and (d). According to (11), we can infer that while β is set as a greater value, the gradient proposition would be greater in the reconstruction results. This means that the prior proposition would be larger, which may result in image oversmoothing and further cause COVID-19 image features missing. In addition, a smaller β cannot remove the sparse sampling artifacts, which can also lead to poor image quality in this case. According to Fig. 12(e) and (f), it can be observed that the parameter γ has a huge impact on the RMSE and SSIM values. Specifically, although a great γ can reduce the errors in some cases to some extent, it can also cause a large jump in terms of SSIM, especially at the end of axial slices. A small γ can result in large RMSE with small SSIM values. It is important to balance in practice.

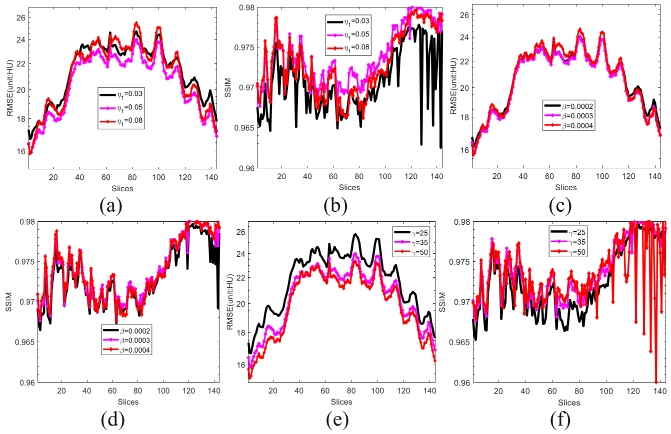

(a) (b) (c)

(d) (e) (f)

Fig. 12. Parameters comparison in terms of RMSE and SSIM. (a) and (b), (c) and (d), (e) and (f) RMSEs and SSIMs with different sets of the parameter η_1, β, and γ, respectively.

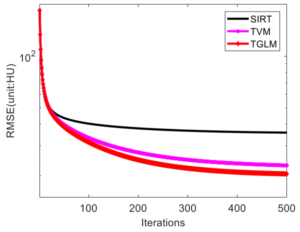

Fig. 13. Convergence curves in terms of RMSEs versus iterations.

3) Convergence and Computational Cost: The mathematical model of TGLM contains the data fidelity and regularization terms. In this study, the tensor gradient L_0-norm enhances the sparsity within the 3-D spatial domain. In addition, the tensor L_0-norm minimization is a nonconvex optimization problem, which also makes it difficult to analyze the convergence of the algorithm. Here, we only numerically study the convergence of the proposed method by using the average RMSE index versus iteration number in Fig. 13. Since the projection is not complete and the result in the exactness of solution is corrupted by artifacts, the RMSE values of SIRT drop off rapidly and then increase slowly [45]. The RMSEs of TVM and our proposed method are strictly decreasing with respect to the iteration number and finally converge to a stable level. In particular, the TGLM can obtain a good solution with the smallest RMSE.

In this study, all the source codes are programmed by MATLAB (2017b) on a PC (16 CPUs at 3.70 GHz, 16.0 GB RAM, and GPU-NVIDIA TITAN Xp, 8.0 GB VRAM) with

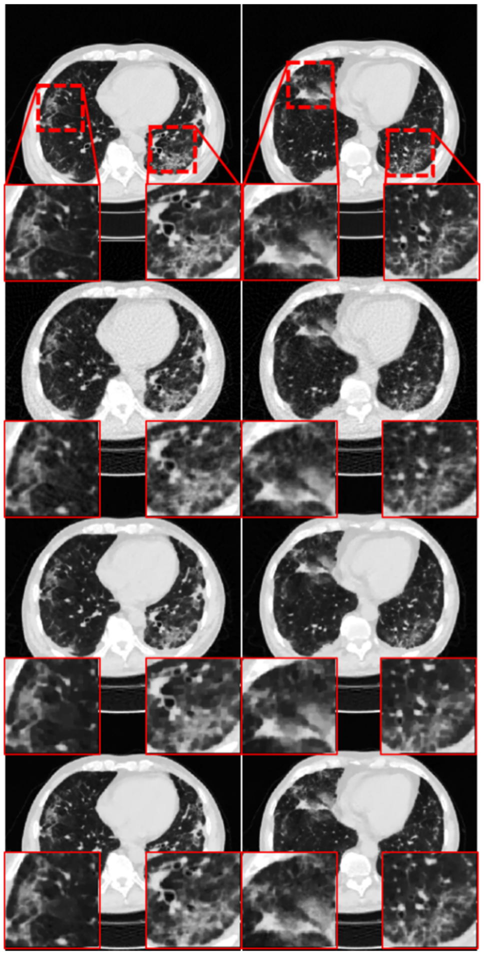

Fig. 14. Reconstructed results for two representative axial slices of case 2. The first–second columns represent 100th and 115th slices, and the first–fourth rows represent the ground truth, SIRT, TVM, and TGLM results and the window is [−1000, 200] HU.

Windows 10. Regarding the computational cost, one iteration for SIRT, TVM, and TGLM methods consumes 26.09, 28.95, and 54.26 s, respectively. The TGLM needs more time than SIRT and TVM methods.

C. Patient #2

Figs. 14 and 15 show some axial slices of patient 2. From these results, one can see that the SIRT results are also corrupted by artifacts. As a result, unique image features are difficult to be discriminated from artifacts. TVM (third rows in Figs. 14 and 15) can improve the reconstructed image quality with artifact reduction to some extent. However, the image edges, image details, and COVID-19 image features are still blurred. Compared with the SIRT and TVM, the proposed TGLM method (fourth row in Figs. 14 and 15) improves image quality with clear image edges and details with visible COVID-19 features. To demonstrate the advantages of the proposed TGLM algorithm, eight ROIs are extracted and magnified in Figs. 14 and 15 to validate these conclusions.

Besides, the 360th coronal slice and 360th sagittal slice are shown in Fig. 16. From Fig. 16, it can be seen that the TVM and TGLM can improve the image quality with reduced artifacts. To further compare the performance of TVM and TGLM, two ROIs are extracted and magnified. From the magnification ROIs results, we can be able to make a conclusion that the TGLM can provide higher image quality than those obtained by the SIRT and TVM.

To further evaluate the developed TGLM method in practice, three radiologists with rich experience in COVID-19 diagnosis are invited to appraise all reconstruct results from worst (0) to best (10) in terms of artifact reduction, resolution, and unique COVID-19 image features preservation. Here, their scores are listed in Table II. It can be observed that the proposed TGLM can obtain the highest scores than competitors. These results can further demonstrate that the proposed TGLM outperforms other methods in practice.

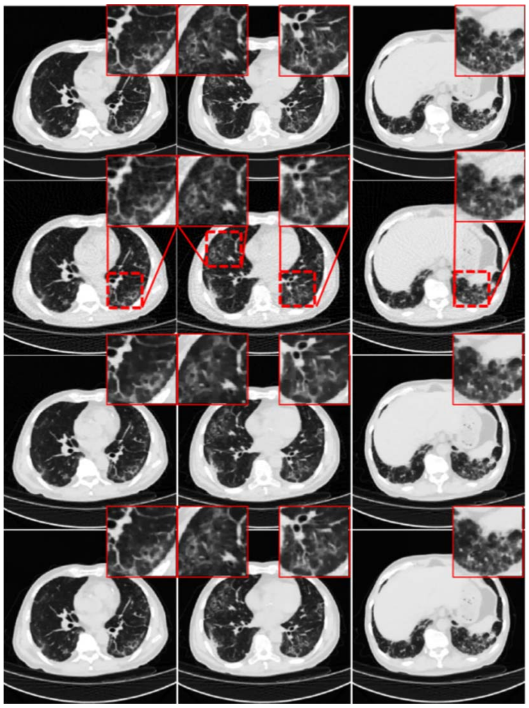

Fig. 15. Reconstructed results for two representative axial slices of case 2. The first–third columns represent 80th, 90, and 135th slices, and the first–fourth rows represent the ground truth, SIRT, TVM, and TGLM results and the window is [−1000, 200] HU.

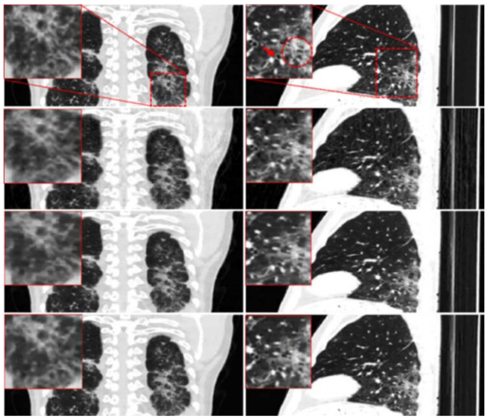

Fig. 16. First and second columns represent reconstructed results from 360th coronal and 360th sagittal slice and their windows are [−1000, 200] and [−1000, 0] HU. The first–fourth rows represent the ground truth, SIRT, TVM, and TGLM results.

TABLE II

SCORES FROM DIFFERENT RADIOLOGISTS WITH DIFFERENT METHODS

Radiologists	Patient	SIRT	TVM	TGLM
#1	#1	5.8	7.6	**9.2**
	#2	6.5	8.4	**9.3**
#2	#1	6.2	8.0	**9.0**
	#2	6.0	8.5	**9.4**
#3	#1	5.5	6.9	**8.9**
	#2	5.0	7.4	**8.8**

V. DISCUSSION AND CONCLUSION

To reduce radiation dose while maintaining high-quality image reconstruction, we developed a TGLM reconstruction method. At first, we propose a tensor gradient L_0-norm regularizer for tensor recovery and smoothing, which can incorporate the multiple dimensions information by counting the nonzeros number of summation of all gradient directions. For CT imaging, it can count the nonzero number within a 3-D volumetric domain rather than a 2-D image. This can benefit to narrow the feasible domain so that a better solution can be obtained. Then, the proposed tensor gradient L_0-norm was incorporated into iteration-type reconstruction to characterize the sparsity of the 3-D domain. The advantages of TGLM can be mainly summarized as the following two aspects. First, the unique image features of patients can be recovered well by exploring volumetric sparsity rather than spatial sparsity by TVM. Therefore, the TGLM can provide accurate detection results even in low-dose case. Second, it has a good ability to preserve image edges with sparse undersamplig artifacts reduction.

Although the TGLM technique can obtain distinguish performance than other comparisons, there are still some limitations that should be addressed in the future. First, TGLM contains three parameters (i.e., η_1, β and γ) and they are optimized manually in this study. The theoretical analyses and optimization are still open problems. In our following work, we will explore the automatic strategies to select different parameters [46], [47]. The L-curve-based adaptive parameter selection methods have demonstrated the great potential of determining regularized parameters for CT imaging [48]. It is feasible to optimize L-curve in our future work.

In summary, we first formulate a tensor gradient L_0-norm for tensor image smoothing and recovery. Then, considering COVID-19 CT imaging features, our proposed TGLM reconstruction method is employed to low-dose CT imaging for COVID-19 patients. Finally, the optimization procedure is designed to recover higher quality of CT images. The experiments on COVID-19 patients demonstrate the advantages of the proposed TGLM method, which will be significant for low-dose CT testing.

APPENDIX A

Since each element is independent of the object function (9), we can further separate it into $I_1 \times I_2 \times \ldots \times I_N$ subproblem. For an arbitrary subproblem, it equals to optimize

$$\begin{aligned}\min_{\boldsymbol{x}(i_1,i_2,\ldots,i_N),\{\mathcal{G}_n(i_1,i_2,\ldots,i_N)\}_{n=1}^N} &\frac{1}{2}\Big\{(\mathcal{Y}(i_1,i_2,\ldots,i_N)\\ &-\mathcal{X}(i_1,i_2,\ldots,i_N))^2+\lambda g((i_1,i_2,\ldots,i_N)\lfloor|\mathcal{G}_1|\\ &+\ldots+|\mathcal{G}_N|\neq 0\rfloor)+\sum_{n=1}^N\beta_n(\mathcal{G}_n(i_1,i_2,\ldots,i_N)\\ &-\partial_{x_n}\mathcal{X}(i_1,i_2,\ldots,i_N)\big)^2\Big\}. \end{aligned}\tag{A1}$$

Furthermore, the object function (A1) can be solved iteratively by updating one variable with other variables fixed.

Updating $\mathcal{X}$: From (A1), $\mathcal{X}$ can be updated by optimizing all $\mathcal{X}(i_1,i_2,\ldots,i_N)$. Again, it can be updated by

$$\min_{\boldsymbol{x}}\frac{1}{2}\left\{(\mathcal{Y}-\mathcal{X})^2+\sum_{n=1}^N\beta_n\|(\mathcal{G}_n)^{(k)}-\partial_{x_n}\mathcal{X}\|_F^2\right\}\tag{A2}$$

where k represents the current iteration number. Equation (A2) is a quadratic function, which can reach a global minimum. Here, the Fourier transform-based method is employed and its solution can be given as

$$\mathcal{X}^{(k+1)}=\mathcal{F}^{-1}\left(\frac{\mathcal{F}(\mathcal{X}^{(k)})+\sum_{n=1}^N\beta_n\mathcal{F}(\partial_{x_n})^*\mathcal{F}(\mathcal{G}_n)}{\mathcal{F}(1)+\sum_{n=1}^N\beta_n\mathcal{F}(\partial_{x_n})^*\mathcal{F}(\partial_{x_n})}\right)\tag{A3}$$

where $\mathcal{F}$, $\mathcal{F}^{-1}$, and $\mathcal{F}^*$ represent the Fourier, inverse Fourier, and complex conjugate Fourier transforms and $\mathcal{F}(1)$ is the Fourier transform of the delta function.

Updating $\{\mathcal{G}_{\boldsymbol{n}}\}_{\boldsymbol{n}=1}^N$: From (A1), we can update $\mathcal{G}_n(i_1,i_2,\ldots,i_N)$ individually. Again, $(i_1,i_2,\ldots,i_N)^{th}$ entry of $\mathcal{G}_n(i_1,i_2,\ldots,i_N)$ can be optimized as

$$\begin{aligned}&\mathcal{J}(i_1,i_2,\ldots,i_N)\\ &=\min_{\{\mathcal{G}_n(i_1,i_2,\ldots,i_N)\}_{n=1}^N}\frac{1}{2}\Bigg\{\lambda g((i_1,i_2,\ldots,i_N)\lfloor|\mathcal{G}_1|+\ldots+|\mathcal{G}_N|\boldsymbol{\neq 0}\rfloor)\\ &\quad+\sum_{n=1}^N\beta_n\big(\mathcal{G}_n(i_1,i_2,\ldots,i_N)-\partial_{x_n}\mathcal{X}(i_1,i_2,\ldots,i_N)^{(k+1)}\big)^2\Bigg\}.\end{aligned}\tag{A4}$$

In fact, $g(\cdot)$ is a binary function when $|\mathcal{G}_1(i_1,i_2,\ldots,i_N)|+\ldots+|\mathcal{G}_N(i_1,i_2,\ldots,i_N)|\neq 0$, $g(\cdot)$ will add 1 and 0 otherwise. The object function of (A4) can reach a minimum under the condition as (A5), shown at the bottom of the page.

The proof of this part can be divided into two cases.

$$\begin{aligned}&(\mathcal{G}_1(i_1,i_2,\ldots,i_N),\ldots,\mathcal{G}_N(i_1,i_2,\ldots,i_N))\\ &\qquad=\begin{cases}(0,\ldots,0), & \left(\sum_{n=1}^N\beta_n\big(\partial_{x_n}\mathcal{X}(i_1,i_2,\ldots,i_N)\big)^2\right)\leq\lambda\\ \big(\partial_{x_1}\mathcal{X}(i_1,i_2,\ldots,i_N),\ldots,\partial_{x_N}\mathcal{X}(i_1,i_2,\ldots,i_N)\big), & \text{otherwise}\end{cases}\end{aligned}\tag{A5}$$

1) When $(\sum_{n=1}^{N}\beta_n(\partial_{x_n}\mathcal{X}(i_1,i_2,\ldots,i_N))^2) \leq \lambda$, nonzero $(\mathcal{G}_1(i_1,i_2,\ldots,i_N),\ldots,\mathcal{G}_N(i_1,i_2,\ldots,i_N))$ can generate

$$\begin{aligned}&\mathcal{J}(i_1,i_2,\ldots,i_N)\\&=\lambda+\sum_{n=1}^{N}\beta_n\big(\mathcal{G}_n(i_1,i_2,\ldots,i_N)-\partial_{x_n}\mathcal{X}(i_1,i_2,\ldots,i_N)^{(k+1)}\big)^2\\&\geq\lambda\geq\sum_{n=1}^{N}\beta_n\big(\partial_{x_n}\mathcal{X}(i_1,i_2,\ldots,i_N)\big)^2.\end{aligned}\tag{A6}$$

When $(\mathcal{G}_1(i_1,i_2,\ldots,i_N),\ldots,\mathcal{G}_N(i_1,i_2,\ldots,i_N))=(0,\ldots,0)$, (A6) can be calculated as

$$J(i_1,i_2,\ldots,i_N)=\sum_{n=1}^{N}\beta_n\big(\partial_{x_n}\mathcal{X}(i_1,i_2,\ldots,i_N)\big)^2 \tag{A7}$$

Compared with (A6) and (A7), one can see that minimum of energy can be reached at $(\mathcal{G}_1(i_1,i_2,\ldots,i_N),\ldots,\mathcal{G}_N(i_1,i_2,\ldots,i_N))=(0,\ldots,0)$.

Algorithm 1

```
Input: Tensor $\mathcal{Y}$, smoothing factors $\beta_1$, $\rho_0$, $\rho_{max}$, $\mathbf{w}$ and $\gamma$
Initialization: $\mathcal{X} \leftarrow \mathcal{Y}$ , $\rho \leftarrow \rho_0$, $k = 1$;
While($\rho < \rho_{max}$)
  do
  Updating $\mathcal{X}^{(k+1)}$ using Eq. (A3);
  Updating all pixels of $\{\mathcal{G}_n\}_{n=1}^{N}$ using Eq. (A5);
  $\rho \leftarrow \gamma\rho$, $k = k + 1$;
end while
Output: $\mathcal{X}$
```

1) When $(\sum_{n=1}^{N}\beta_n(\partial_{x_n}\mathcal{X}(i_1,i_2,\ldots,i_N))^2)>\lambda$ and $(\mathcal{G}_1(i_1,i_2,\ldots,i_N),\ldots,\mathcal{G}_N(i_1,i_2,\ldots,i_N)) = (0,\ldots,0)$, (A7) is true. For $(\mathcal{G}_1(i_1,i_2,\ldots,i_N),\ldots,\mathcal{G}_N(i_1,i_2,\ldots,i_N)) \neq (0,\ldots,0)$, its minimum of energy can reach λ. Thus, the minimum energy of the object function of (A5) $J(i_1,i_2,\ldots,i_N)=\lambda$ at $(\partial_{x_1}\mathcal{X}(i_1,i_2,\ldots,i_N),\ldots,\partial_{x_N}\mathcal{X}(i_1,i_2,\ldots,i_N))$. ■

Similar to the 2-D image gradient L$_0$-norm minimization [26], the iteration process of tensor gradient L$_0$-norm-based tensor recovery algorithm is listed in Algorithm I. ρ is an automatical updation parameter during the iteration process with a small initial $\rho_0 = 2 * (\sum_{n=1}^{N}\beta_n)/N$ by a multiplier γ. The maximum of ρ is set as $\rho_{\max}$ and here, it is 10^5. $\beta_n(n = 1,\ldots,N)$ are coupling factors to control the proposition components from the nth dimension. To unify $\beta_n(n = 1,\ldots,N)$ parameters, each β_n can be written as $\mathbf{w}\beta$ and $\mathbf{w} = [w_1,\ldots,w_N]^T\beta$. This means that we can adjust w_n to change β_n.

APPENDIX B

Regarding the optimization of (14), it can be alternatively updated with one variable one time. In fact, we can separate it into three subproblems

$$\min_{z}\frac{1}{2}\|\mathcal{M}\mathbf{z}-\mathcal{P}\|_F^2+\frac{\eta_1}{2}\|\mathcal{Z}-\mathcal{W}^{(k_1)}-\mathcal{V}^{(k_1)}\|_F^2 \tag{B1}$$

$$\min_{w}\eta\|\nabla\mathcal{W}\|_0+\frac{\eta_1}{2}\|\boldsymbol{\mathcal{Z}^{(k_1+1)}-\mathcal{W}-\mathcal{V}^{(k_1)}}\|_{\boldsymbol{F}}^{\mathbf{2}} \tag{B2}$$

$$\hat{\mathcal{V}}^{(k_1+1)}=\mathcal{V}^{(k_1)}-\mathcal{Z}^{(k_1+1)}+\mathcal{W}^{(k_1+1)} \tag{B3}$$

where k_1 represent the current iteration. $\mathcal{Z}^{(k_1+1)}$, $\mathcal{W}^{(k_1+1)}$, and $\mathcal{V}^{(k_1+1)}$ can be iteratively updated so that we can obtain an optimized solution. Equation (B1) can be solved as

$$\begin{aligned}&\hat{\mathcal{Z}}_{j_1j_2j_3}^{(k_1+1)}\\&=\mathcal{Z}_{j_1j_2j_3}^{(k_1)}\\&\quad-\frac{\big[\mathrm{fold}\big(\mathcal{M}^T(\mathcal{M}\mathbf{z}-\mathcal{P})\big)\big]_{j_1j_2j_3}+\eta_1\Big[\hat{\mathcal{Z}}^{(k_1)}-\mathcal{W}^{(k_1)}-\mathcal{V}^{(k_1)}\Big]_{j_1j_2j_3}}{\big[\mathrm{fold}\big(\mathcal{M}^T\mathcal{M}\big)\big]_{j_1j_2j_3}+\eta_1}\end{aligned}\tag{B4}$$

where fold$(\cdot)$ represents fold the vector into a tensor, and the symbol $[\cdot]_{j_1j_2j_3}$ indicates the $(j_1, j_2, j_3)^{th}$ element of a third-order tensor. $\mathcal{M}^T$ indicates the transpose of $\mathcal{M}$. Regarding the object function of (B2), it has been discussed in Appendix A.

The overall flowchart of the proposed approach is summarized in Algorithm II. In this study, β_1, β_2, and β_3 are set as the same value. For different applications, it is not easy to find the most suitable parameters, the input of tensor gradient L-norm is normalized to [0,1], and the denormalization operator should be used for output results.

Algorithm 2 TGLM Algorithm

```
Input: $\mathcal{P}$, the parameters of $\eta_1$, $\beta$ and $\gamma$ ;
Initialization: $\{\mathcal{Z}^{(0)}, \mathcal{W}^{(0)}, \mathcal{V}^{(0)}\} \leftarrow \mathbf{0}, k_1 = 0$;
Whilenot convergence
  do
Updating $\hat{\mathcal{Z}}^{(k_1+1)}$ using Eq. (B4);
Normalizing $\mathcal{Z}^{(k_1+1)}-\mathcal{V}^{(k_1)}$;
Updating $\hat{\mathcal{W}}^{(k_1+1)}$ using Algorithm I;
Denormalizing $\hat{\mathcal{W}}^{(k_1+1)}$;
Updating $\hat{\mathcal{V}}^{(k_1+1)}$ utilizing Eq. (B3);
$k = k+1$;
End while
Output: $\mathcal{Z}$
```

REFERENCES

[1] Y. Han and J. C. Ye, "Framing U-Net via deep convolutional framelets: Application to sparse-view CT," *IEEE Trans. Med. Imag.*, vol. 37, no. 6, pp. 1418–1429, Jun. 2018.

[2] J. Huang *et al.*, "Iterative image reconstruction for sparse-view CT using normal-dose image induced total variation prior," *PLoS ONE*, vol. 8, no. 11, Nov. 2013, Art. no. e79709.

[3] W. Wu *et al.*, "Stabilizing deep tomographic reconstruction networks," 2020, *arXiv:2008.01846*. [Online]. Available: http://arxiv.org/abs/2008.01846

[4] H. K. Tuy, "An inversion formula for cone-beam reconstruction," *SIAM J. Appl. Math.*, vol. 43, no. 3, pp. 546–552, Jun. 1983.

[5] S. Eda, K. Kubo, K. Fujimoto, Y. Matsuzawa, M. Sekiguchi, and F. Sakai, "The relations between expiratory chest CT using helical CT and pulmonary function tests in emphysema," *Amer. J. Respiratory Crit. Care Med.*, vol. 155, no. 4, pp. 1290–1294, 1997.

[6] T. Gorycki, I. Lasek, K. Kamiński, and M. Studniarek, "Evaluation of radiation doses delivered in different chest CT protocols," *Polish J. Radiol.*, vol. 79, p. 1, Mar. 2014.

[7] D. Kalasova *et al.*, "Characterization of a laboratory-based X-ray computed nanotomography system for propagation-based method of phase contrast imaging," *IEEE Trans. Instrum. Meas.*, vol. 69, no. 4, pp. 1170–1178, Apr. 2020.

[8] G. Kim *et al.*, "Projection-based dual-energy digital tomosynthesis and its image characteristics," *Instrum. Sci. Technol.*, vol. 47, no. 3, pp. 248–263, May 2019.

[9] Y. Chang, L. Yan, M. Chen, H. Fang, and S. Zhong, "Two-stage convolutional neural network for medical noise removal via image decomposition," *IEEE Trans. Instrum. Meas.*, vol. 69, no. 6, pp. 2707–2721, Jun. 2020.

[10] M. Xu, D. Hu, F. Luo, F. Liu, S. Wang, and W. Wu, "Limited angle X ray CT reconstruction using image gradient ℓ_0-norm with dictionary learning," *IEEE Trans. Radiat. Plasma Med. Sci.*, vol. 5, no. 1, pp. 78–87, Jan. 2021.

[11] S. Wang, W. Wu, J. Feng, F. Liu, and H. Yu, "Low-dose spectral CT reconstruction based on image-gradient L_0-norm and adaptive spectral PICCS," *Phys. Med. Biol.*, vol. 65, no. 24, Dec. 2020, Art. no. 245005.

[12] Q. Xu, H. Yu, X. Mou, L. Zhang, J. Hsieh, and G. Wang, "Low-dose X-ray CT reconstruction via dictionary learning," *IEEE Trans. Med. Imag.*, vol. 31, no. 9, pp. 1682–1697, Sep. 2012.

[13] W. Wu, P. Chen, S. Wang, V. Vardhanabhuti, F. Liu, and H. Yu, "Image-domain material decomposition for spectral CT using a generalized dictionary learning," *IEEE Trans. Radiat. Plasma Med. Sci.*, early access, May 26, 2020, doi: 10.1109/TRPMS.2020.2997880.

[14] Z. Tian, X. Jia, K. Yuan, T. Pan, and S. B. Jiang, "Low-dose CT reconstruction via edge-preserving total variation regularization," *Phys. Med. Biol.*, vol. 56, no. 18, p. 5949, 2011.

[15] D. Wu, K. Kim, G. El Fakhri, and Q. Li, "Iterative low-dose CT reconstruction with priors trained by artificial neural network," *IEEE Trans. Med. Imag.*, vol. 36, no. 12, pp. 2479–2486, Dec. 2017.

[16] J. Liu *et al.*, "Discriminative feature representation to improve projection data inconsistency for low dose CT imaging," *IEEE Trans. Med. Imag.*, vol. 36, no. 12, pp. 2499–2509, Dec. 2017.

[17] X. Yin *et al.*, "Domain progressive 3D residual convolution network to improve low-dose CT imaging," *IEEE Trans. Med. Imag.*, vol. 38, no. 12, pp. 2903–2913, Dec. 2019.

[18] J. Liu *et al.*, "Deep iterative reconstruction estimation (DIRE): Approximate iterative reconstruction estimation for low dose CT imaging," *Phys. Med. Biol.*, vol. 64, no. 13, Jul. 2019, Art. no. 135007.

[19] H. Chen *et al.*, "Low-dose CT with a residual encoder-decoder convolutional neural network," *IEEE Trans. Med. Imag.*, vol. 36, no. 12, pp. 2524–2535, Dec. 2017.

[20] R. C. Nelson, S. Feuerlein, and D. T. Boll, "New iterative reconstruction techniques for cardiovascular computed tomography: How do they work, and what are the advantages and disadvantages?" *J. Cardiovascular Comput. Tomogr.*, vol. 5, no. 5, pp. 286–292, Sep. 2011.

[21] W. Wu, D. Hu, K. An, S. Wang, and F. Luo, "A high-quality photon-counting CT technique based on weight adaptive total-variation and image-spectral tensor factorization for small animals imaging," *IEEE Trans. Instrum. Meas.*, vol. 70, pp. 1–14, 2021.

[22] D. Kim, D. Pal, J.-B. Thibault, and J. A. Fessler, "Accelerating ordered subsets image reconstruction for X-ray CT using spatially nonuniform optimization transfer," *IEEE Trans. Med. Imag.*, vol. 32, no. 11, pp. 1965–1978, Nov. 2013.

[23] J. Leipsic *et al.*, "Estimated radiation dose reduction using adaptive statistical iterative reconstruction in coronary CT angiography: The ERASIR study," *Amer. J. Roentgenol.*, vol. 195, no. 3, pp. 655–660, Sep. 2010.

[24] S. Do, W. C. Karl, M. K. Kalra, T. J. Brady, and H. Pien, "A variational approach for reconstructing low dose images in clinical helical CT," in *Proc. IEEE Int. Symp. Biomed. Imag.: Nano Macro*, 2010, pp. 784–787.

[25] H. Nam *et al.*, "Tensor framelet based iterative image reconstruction algorithm for low-dose multislice helical CT," *PLoS ONE*, vol. 14, no. 1, Jan. 2019, Art. no. e0210410.

[26] L. Xu, C. Lu, Y. Xu, and J. Jia, "Image smoothing via L_0 gradient minimization," in *Proc. SIGGRAPH Asia Conf.*, 2011, pp. 1–12.

[27] Y. E. Salehani, S. Gazor, I. M. Kim, and S. Yousefi, "ℓ_0-norm sparse hyperspectral unmixing using arctan smoothing," *Remote Sens.*, vol. 8, no. 3, p. 187, 2016.

[28] W. Wu, Y. Zhang, Q. Wang, F. Liu, P. Chen, and H. Yu, "Low-dose spectral CT reconstruction using image gradient ℓ_0–norm and tensor dictionary," *Appl. Math. Model.*, vol. 63, pp. 538–557, Nov. 2018.

[29] D. Hu *et al.*, "SISTER: Spectral-image similarity-based tensor with enhanced-sparsity reconstruction for sparse-view multi-energy CT," *IEEE Trans. Comput. Imag.*, vol. 6, pp. 477–490, 2020.

[30] W. Yu, C. Wang, X. Nie, M. Huang, and L. Wu, "Image reconstruction for few-view computed tomography based on ℓ_0 sparse regularization," *Procedia Comput. Sci.*, vol. 107, pp. 808–813, 2017.

[31] F. Luo, L. Zhang, B. Du, and L. Zhang, "Dimensionality reduction with enhanced hybrid-graph discriminant learning for hyperspectral image classification," *IEEE Trans. Geosci. Remote Sens.*, vol. 58, no. 8, pp. 5336–5353, Aug. 2020.

[32] F. Luo, L. Zhang, X. Zhou, T. Guo, Y. Cheng, and T. Yin, "Sparse-adaptive hypergraph discriminant analysis for hyperspectral image classification," *IEEE Geosci. Remote Sens. Lett.*, vol. 17, no. 6, pp. 1082–1086, Jun. 2020.

[33] W. Wu, F. Liu, Y. Zhang, Q. Wang, and H. Yu, "Non-local low-rank cube-based tensor factorization for spectral CT reconstruction," *IEEE Trans. Med. Imag.*, vol. 38, no. 4, pp. 1079–1093, Apr. 2019.

[34] W. Wu, P. Chen, V. V. Vardhanabhuti, W. Wu, and H. Yu, "Improved material decomposition with a two-step regularization for spectral CT," *IEEE Access*, vol. 7, pp. 158770–158781, 2019.

[35] X. Jiang, S. Rayner, and M. H. Luo, "Does SARS-CoV-2 has a longer incubation period than SARS and MERS?" *J. Med. Virol.*, vol. 92, no. 5, pp. 476–478, 2020.

[36] M. Chung *et al.*, "CT imaging features of 2019 novel coronavirus (2019-nCoV)," *Radiol.*, vol. 295, no. 3, 2020, Art. no. 200230.

[37] H. Xue, S. Zhang, and D. Cai, "Depth image inpainting: Improving low rank matrix completion with low gradient regularization," *IEEE Trans. Image Process.*, vol. 26, no. 9, pp. 4311–4320, Sep. 2017.

[38] C. Xie *et al.*, "Discrimination of pulmonary ground-glass opacity changes in COVID-19 and non-COVID-19 patients using CT radiomics analysis," *Eur. J. Radiol. Open*, vol. 7, 2020, Art. no. 100271.

[39] J. Trampert and J. J. Leveque, "Simultaneous iterative reconstruction technique: Physical interpretation based on the generalized least squares solution," *J. Geophys. Res.: Solid Earth*, vol. 95, no. B8, pp. 12553–12559, 1990.

[40] H. Yu, G. Wang, "Compressed sensing based interior tomography," *Phys. Med. Biol.*, vol. 54, no. 9, p. 2791, 2009.

[41] W. Wu, H. Yu, C. Gong, and F. Liu, "Swinging multi-source industrial CT systems for aperiodic dynamic imaging," *Opt. Exp.*, vol. 25, no. 20, pp. 24215–24235, 2017.

[42] Q. Xu *et al.*, "Image reconstruction for hybrid true-color micro-CT," *IEEE Trans. Biomed. Eng.*, vol. 59, no. 6, pp. 1711–1719, Jun. 2012.

[43] S. Tan *et al.*, "Tensor-based dictionary learning for dynamic tomographic reconstruction," *Phys. Med. Biol.*, vol. 60, no. 7, p. 2803, 2015.

[44] Y. Zhang, X. Mou, G. Wang, and H. Yu, "Tensor-based dictionary learning for spectral CT reconstruction," *IEEE Trans. Med. Imag.*, vol. 36, no. 1, pp. 142–154, Jan. 2017.

[45] W. Wu, Y. Zhang, Q. Wang, F. Liu, F. Luo, and H. Yu, "Spatial-spectral cube matching frame for spectral CT reconstruction," *Inverse Problems*, vol. 34, no. 10, Oct. 2018, Art. no. 104003.

[46] K. Khare, C. J. Hardy, K. F. King, P. A. Turski, and L. Marinelli, "Accelerated MR imaging using compressive sensing with no free parameters," *Magn. Reson. Med.*, vol. 68, no. 5, pp. 1450–1457, Nov. 2012.

[47] P. C. Hansen and D. P. O'Leary, "The use of the L-Curve in the regularization of discrete ill-posed problems," *SIAM J. Sci. Comput.*, vol. 14, no. 6, pp. 1487–1503, Nov. 1993.

[48] C. Gong and L. Zeng, "Adaptive iterative reconstruction based on relative total variation for low-intensity computed tomography," *Signal Process.*, vol. 165, pp. 149–162, Dec. 2019.

Weiwen Wu was born in China in 1991. He received the Ph.D. degree in optoelectronic engineering from Chongqing University, Chongqing, China, in 2019.

From 2017 to 2018, he was a Joint-training Ph.D. student with the University of Massachusetts Lowell with Dr. Hengyong Yu. From 2019 to 2020, he was a Post-Doctoral Fellow with The University of Hong Kong, Hong Kong, with Dr. Varut Vardhanabhuti. Since 2020, he has been a Post-Doctoral Fellow with the Rensselaer Polytechnic Institute, Troy, NY, USA, with Prof. Ge Wang. He has published more than 30 academic articles and abstracts in peer-reviewed publications. His research interests include deep learning, compressed sensing, X-ray system design, image reconstruction, dynamic bowtie, and material decomposition.

Dr. Wu was a Guest Editor of the *EURASIP Journal on Advances in Signal Processing*. His awards and honors include the Chinese Scholarship Council and the Non-destructive Testing Scholarship in 2019.

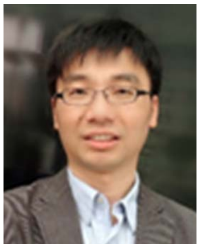

Jun Shi (Associate Member, IEEE) received the B.S. and Ph.D. degrees from the Department of Electronic Engineering and Information Science, University of Science and Technology of China, Hefei, China, in 2000 and 2005, respectively.

In 2005, he joined the School of Communication and Information Engineering, Shanghai University, Shanghai, China, where he has been a Professor since 2015. From 2011 to 2012, he was a Visiting Scholar with the University of North Carolina at Chapel Hill, Chapel Hill, NC, USA. His current research interests include machine learning in medical imaging.

Hengyong Yu (Senior Member, IEEE) received the bachelor's degree in information science and technology, the bachelor's degree in computational mathematics, and the Ph.D. degree in information and communication engineering from Xi'an Jiaotong University, in 1998, 1998, and 2003, respectively.

He is currently a Full Professor and the Director of the Imaging and Informatics Lab, Department of Electrical and Computer Engineering, University of Massachusetts Lowell, Lowell, MA, USA. His interests include medical imaging with an emphasis on CT and medical image processing and analysis. He has authored or coauthored more than 150 peer-reviewed journal papers and more than 120 conference proceedings/abstracts. According to Google Scholar Citation, his H-index is 39 and i10-index is 96.

Dr. Yu is the founding Editor-in-Chief of *JSMBiomedicalImaging Data Papers*, serves as an Editorial Board Member for IEEE ACCESS, *Signal Processing*, *CT Theory and Applications*, and so on. In January 2012, he received the NSF CAREER Award for the development of CS-based interior tomography.

Weifei Wu was born in Hunan, China, in 1985. He received the B.S. degree from the Medical College, Yangtze University, Jingzhou, China, in 2010, the M.S. degree from the Medical College, Nanjing University, Nanjing, China, in 2013, and the Ph.D. degree from the Medical College, Wuhan University, Wuhan, China, in 2019.

In 2017, he obtained the Young Grant from the National Natural Science Foundation of China. He is currently a Clinical Doctor with The First People's Hospital of Yichang, Yichang, China. His research interests include CT image analysis, MRI reconstruction, clinical study including mechanism, and treatment of nerve injury. He is a reviewer of the Spine journal, IJS journal, and so on.

Varut Vardhanabhuti received the medical degree from Guy's, King's, and St Thomas' School of Medicine at King's College, London, U.K., in 2005 and the Ph.D. degree in iterative reconstruction in CT during his training from the Peninsula College of Medicine and Dentistry, Plymouth, U.K.

He had subsequent training in London, Oxford, Plymouth, Exeter, and completed his Radiology training as a Fellow at Imperial College London, London. He is currently a Clinical Assistant Professor with the Department of Diagnostic Radiology, Li Ka Shing Faculty of Medicine, The University of Hong Kong, Hong Kong. He engages with various research projects relating to medical imaging, with the goal of early clinical translation to benefits patients. He worked on the Scientific Editorial Board in the CT section in European Radiology. He has published more than 90 academic papers and abstracts in peer-reviewed publications.